Supplementary Material: Laser Brain Cancer Surgery Guided by Optical Coherence Tomography

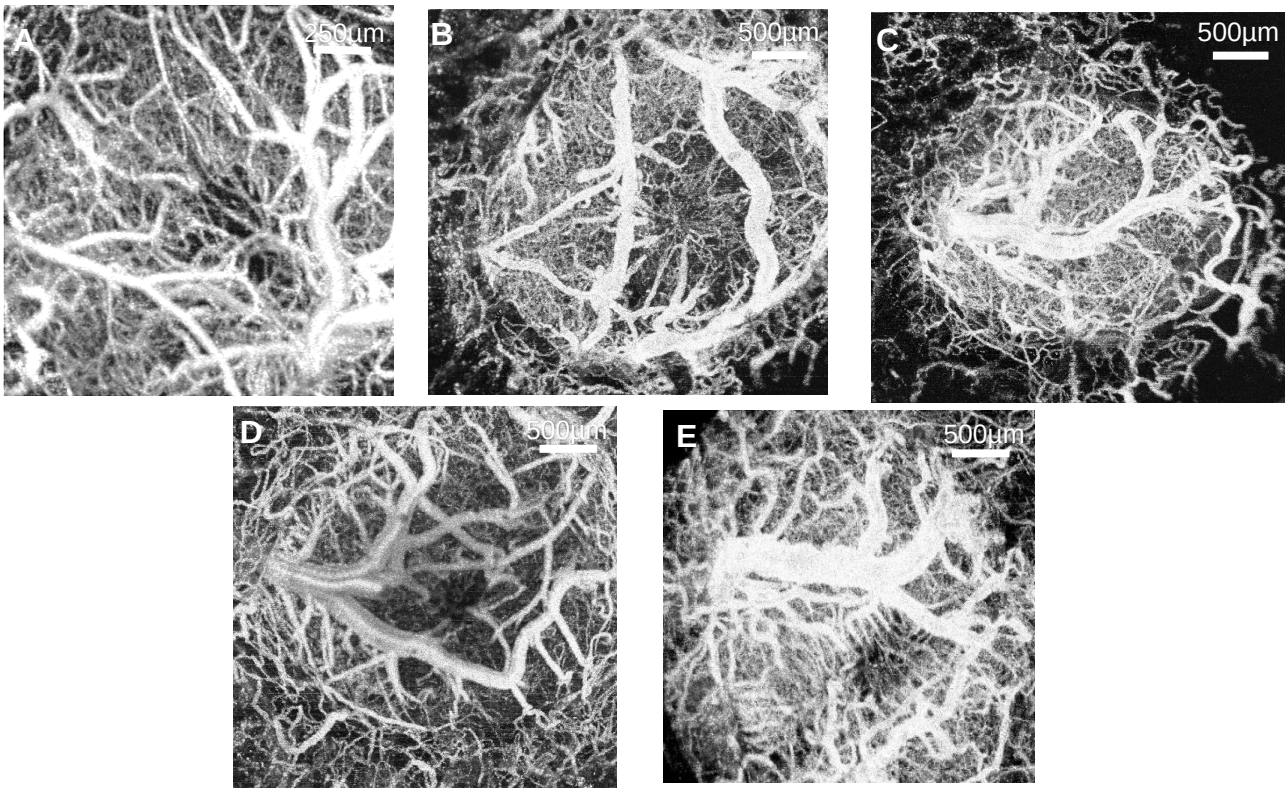

Figure S1. Angiography images computed using described methodology (Section 2). Panel A, B, C, D and E correspond to mice #1, #2, #3, #4 and #5, respectively.

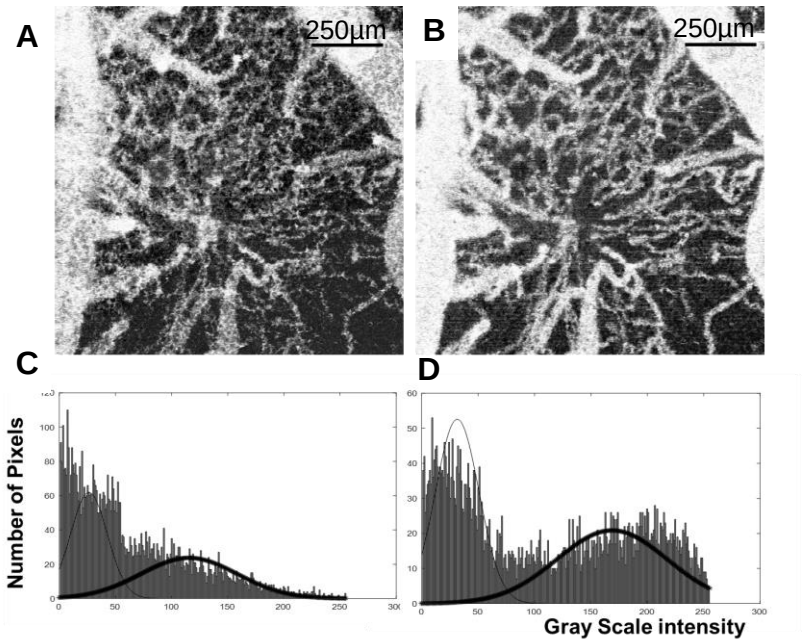

Figure S2. A, B) Angiography image contrast improvement (mouse #2). A-scan interleaving improves vasculature contrast (Panel B compared to Panel A) without loss in spatial resolution. C, D) Histograms of angiography images in A, B respectively. Gaussian distributions of signal (thin solid line) and background (asterisk line) levels. See text for description.

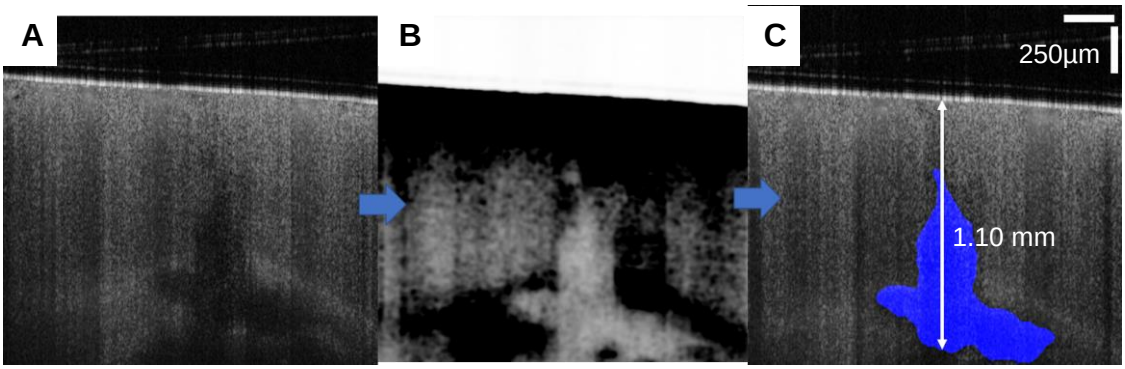

Figure S3. A) Raw intensity image (-30dB to 25dB grayscale). B) Calculated attenuation coefficient image (inverted grayscale to highlight regions of low attenuation corresponding to tumor regions as well as shadows from large blood vessels. C) Overlay of intensity and masked, thresholded attenuation image.

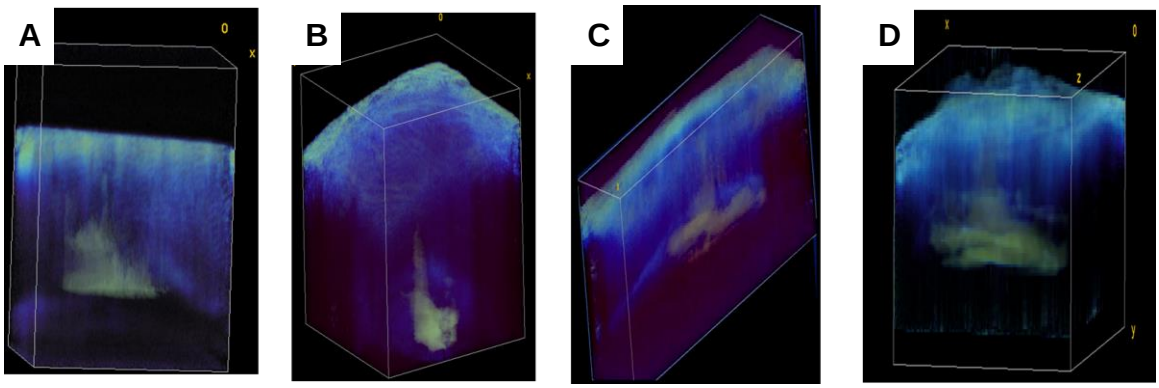

Figure S4. Rendered tumor volumes (yellow, attenuation coefficient less than $5.7mm^{-1}$) overlaid on OCT intensity (blue). Panels A, B, C and D correspond to mice #1, #2, #3, #5. For Panel C, the volume stack was reduced from $3.5 \times 3.5 \times 3mm^3$ (Panels A, B and D) to $3.5 \times 1.75 \times 3mm^3$ for better tumor visualization. In all mice imaged, tumors occupied a characteristic columnar region along the needle track and a wider region along the corpus callosum/hippocampus (for mouse #4 refer to Figure 4 Panel B).

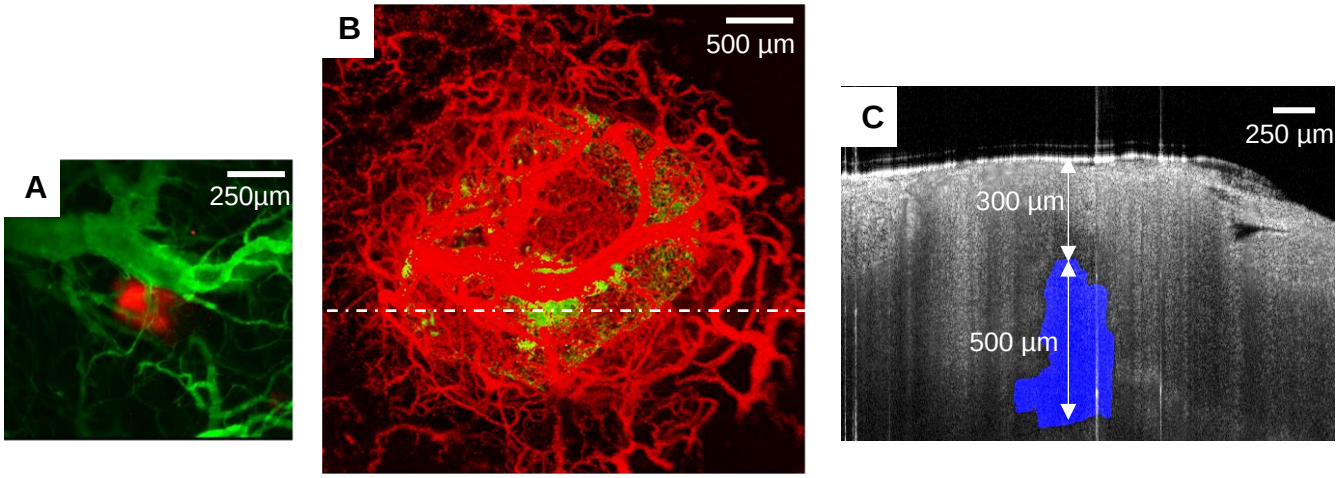

Figure S5. A) Maximum intensity Z-projection of fluorescence confocal microscopy. B) OCT derived Z-projection of vasculature (red) and tumor (green). C) Cross-section in Panel B (dashed line) where tumor location (blue) is overlaid on grayscale OCT intensity image. All images correspond to mouse #3.

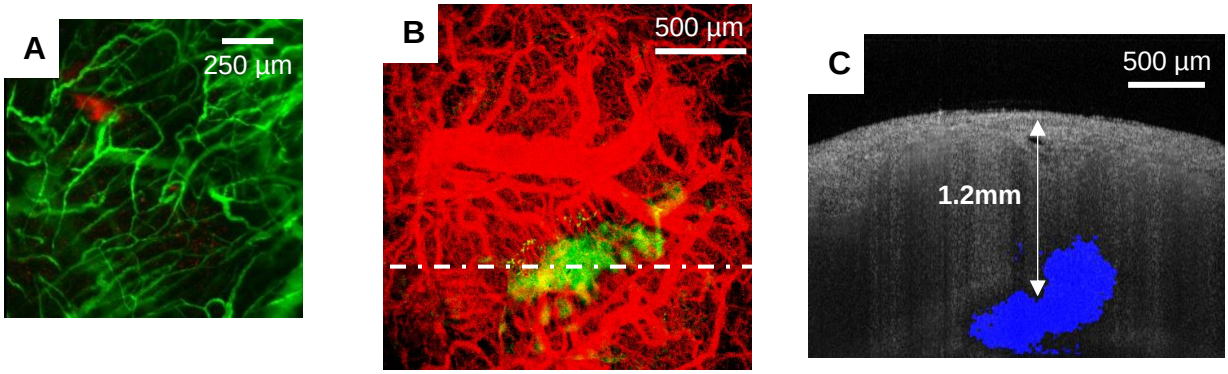

Figure S6. A) Maximum intensity Z-projection of fluorescence confocal microscopy. B) OCT derived Z-projection of vasculature (red) and tumor (green). Cross-section in Panel B (dashed line) where tumor location (blue) is overlaid on grayscale OCT intensity image. All images correspond to mouse #5.

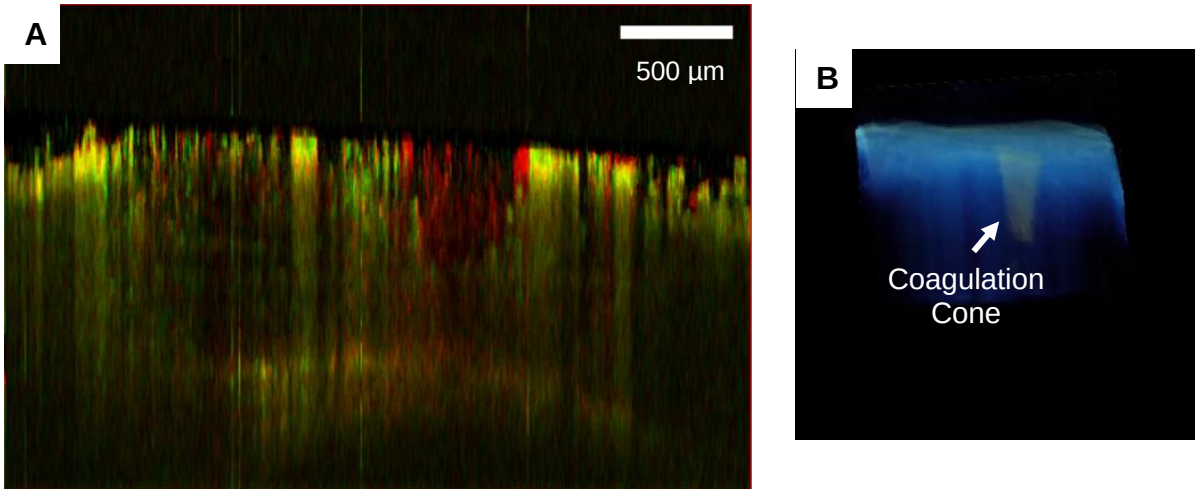

Figure S7. A) Superposed angiography B-scan of murine brain with pre(red)- and post(green)-coagulation B-scans overlaid. Coagulated regions remain red, whereas regions with normal blood flow are yellow (red and green). B) Rendered volume ($3.5 \times 3.5 \times 3$ mm^3) of thulium (Tm) laser coagulation cone indicated. All images correspond to mouse #2.

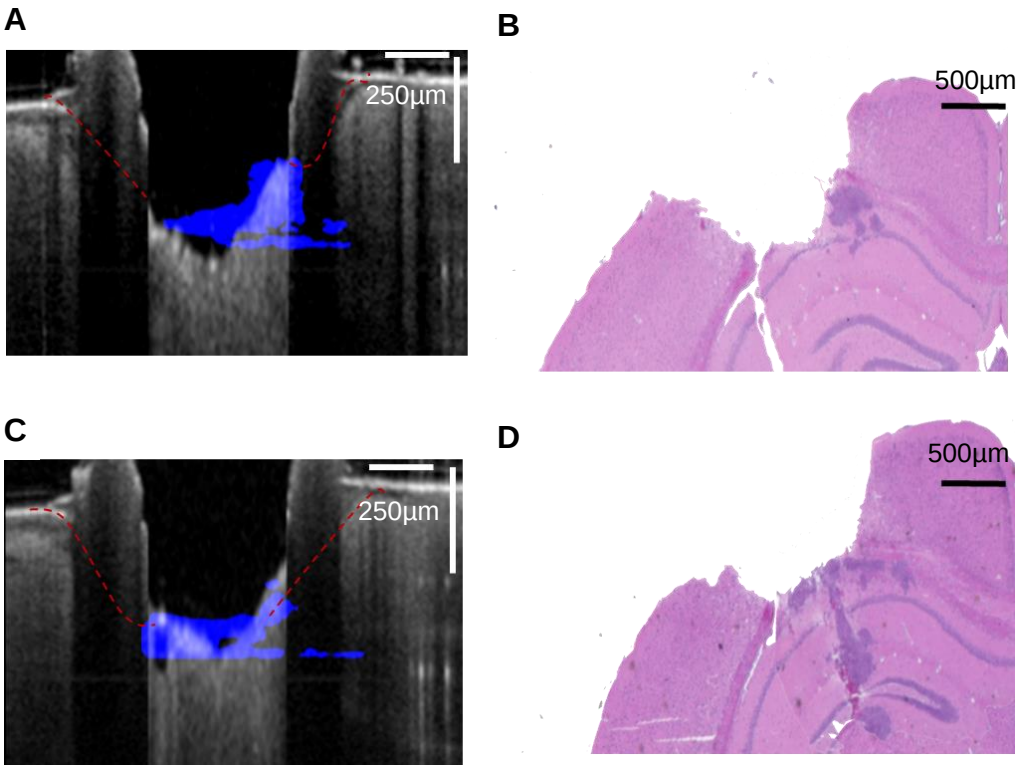

Figure S8. A,C) Post-ablation B-scans (gray) superposed with pre-ablation tumor regions (blue). Cross sections are adjacent to those in Figure 4E. B,D) Corresponding histology sections. All images correspond to mouse #4

Advantages of laser surgery and OCT image guidance: The reported benchtop system incorporates OCT imaging for guidance and provides complementary lasers that can effectively perform image-guided coagulation and ablation.

Emission wavelength of the erbium-doped yttrium aluminum garnet laser (Er:YAG, 2.94 µm) coincides with the absolute water absorption spectral peak [1, 2]. Since soft tissue consists predominantly of water, Er:YAG laser tissue ablation is energy efficient and precise. For tissue composed of 75% water, the absorption coefficient at 2.94 µm is approximately 990 mm^{-1} (absorption depth 1 µm), which allows for precise tissue removal with minimal non-specific damage. These factors make the Er:YAG laser a good candidate for precise tissue ablation.

Despite this advantage, the Er:YAG laser is seldom used for surgical procedures other than skin resurfacing due to less-than-optimal delivery devices and poor hemostasis capability. To coagulate a blood vessel, nearly two-thirds of the cross-section must be transiently heated by 55°C. An ideal coagulation laser should have an absorption depth equal to or larger than diameter of the largest caliber blood vessel in the target tissue. For example, the CO_2 (10.6 µm) laser provides good ablation precision (10 µm absorption depth), but similar to the Er:YAG laser can result in bleeding that must be stopped. A thulium (Tm) laser, however, can rapidly increase the cross-section temperature by 55°C degrees and has

an absorption depth of approximately 125 μm. These parameters make Tm laser irradiation a candidate for blood vessel coagulation [3, 4].

The imaging technique needed to guide surgery must provide rapid feedback in vivo to monitor tumor microenvironment and help control laser-tissue interactions. Without proper feedback, laser-tissue interactions can result in non-specific damage to sensitive structures such as nerves and micro-vessels. OCT is a broadband, light-based imaging modality that bridges the gap between techniques that produce subcellular resolution (2-6 μm) and alternative techniques, such as ultrasonography, microCT and MRI, which have coarser resolutions (150-1000 μm) [4]. Due to the relatively small numerical aperture and entirely intrinsic mechanisms of scattering contrast, OCT is able to measure and monitor tumor angiogenesis, tissue viability, vascular/tumor progression and response to anticancer therapy [5, 6].

A combination of high-resolution, rapid-feedback OCT with a surgical pulsed fiber laser offers advantages over conventional surgical systems. A detailed description of OCT data processing to obtain angiography and attenuation-based tumor renderings and images is outlined below. Additionally, penetration depth limitation of confocal imaging for isolating tumor locations is presented. Finally, supporting data on laser coagulation and murine brain cancer tumor ablation are presented.

Optical coherence tomography (OCT) derived angiography:

Most OCT-based angiography approaches quantify an average decorrelation observed within a depth window of an A-scan over a number of repetitions [7–13]. For sufficient contrast, A-scan sampling times must equal or exceed the expected decorrelation time of moving red blood cells. Considering A-scan rate of current swept source lasers (100-250 kHz), appropriate decorrelation times for B-scan sampling have been successfully demonstrated to image blood flow [7–13]. Split spectrum methodologies [7] trade-off longitudinal resolution (up to 3 times) to improve SNR with good performance observed at about nine spectral intervals [8]. Other amplitude decorrelation techniques [9-12] require an increase in number of B-scan repetitions with two-dimensional kernels to improve SNR, thus resulting in slower processing times. Increase in processing time for amplitude decorrelation techniques [7-12] depend on number of repetitions and spectral intervals. Complex domain techniques [13] analyze A-scan data, preserving the lateral (XY) resolution of flow contrast while providing faster processing times. Complex domain methodologies, however, require approaches to mitigate SNR loss caused by phase noise, that can originate in scan-to-scan variations in swept source lasers [7]. Finally, imaging times on the order of less than two minutes are desirable for many surgical applications.

Considering these constraints, our system recorded eight consecutive B-scans yielding seven decorrelation pairs to construct angiography images. An optimal B-scan time separation for good vasculature contrast in the murine brain was found to be 5-7ms. The standard amplitude decorrelation algorithm reported previously [9], [12] was modified by performing an averaging step before the decorrelation calculation, whereby neighboring

frequencies of the OCT A-scan interferogram were averaged in the optical frequency domain to improve SNR. Although this intra-A-scan averaging theoretically reduces imaging depth, the primary limiting factor for OCT light penetration in tissues is scattering. Thus, SNR enhancement was achieved with no effective loss in image resolution, depth or acquisition time. Although this SNR enhancement introduces a small computational increase in the A-scan decorrelation calculation, this is offset by a reduction in number of A-scan data points. For this work, we averaged interference fringe intensity of neighboring optical frequency data points in the interferogram to produce final A-scans, $\bar{A}$, which were used to calculate decorrelation ($D(z)$, Eq 1). The quantity *w(l)* represented the moving A-scan window of size (*2L+1*), *M* was the number of repetitions and *t*, *t+1* represented adjacent time indices of B-scan repetitions. Decorrelations were computed and projected along the depth dimension (*z*) to form a two-dimensional (*xy*) angiography image of the vasculature.

Angiography images were computed in this manner for all mice (Figure S1). Panels A and B of Figure S2 show the contrast enhancement achieved with A-scan interleaving. To quantify and validate contrast enhancement, gaussian distributions of signal (thin solid-line Panel C,D) and background pixels (asterisks-line Panel C,D) were determined for angiography images in Panels A and B of Figure S2. Due to a substantially wider separation between signal/background gaussian distributions (Panel D, Figure S2) an angiography image with enhanced contrast was obtained (Panel B).

$$D(z)=\sqrt{1-\frac{\sum_{0}^{M-1}\left[\sum_{-L}^{L} w(l)\bar{A}(z-l,t)\bar{A}(z-l,t+1)\right]}{\sum_{0}^{M-1}\left[\sum_{-L}^{L} w(l)\frac{1}{2}\left[\bar{A}(z-l,t)^2+\bar{A}(z-l,t+1)^2\right]\right]}} \qquad \text{Eq.1}$$

Attenuation analysis for tumor identification: Attenuation coefficient images reflect intrinsic tissue scattering and absorption properties at the OCT imaging wavelength. Attenuation coefficient images are objective, quantitative data and therefore can help determine more broadly applicable threshold values. Kut et. al. [14] determined sensitivity and specificity values as compared to histology. Using a threshold attenuation coefficient value of 5.5 mm^{-1}, he demonstrated a sensitivity of 92% and specificity of 100% for high-grade, ex-vivo human brain cancer samples (n=7) and a sensitivity of 100% and specificity of 80% for low-grade, ex-vivo human brain cancer samples (n=9) [14]. This compared favorably to surgeon classification performance of sensitivity/specificity of 50/100% for high-grade and 40/100% for low-grade brain cancer samples as determined during surgery.

We followed the method first reported by Vermeer et al [15] to convert OCT data to attenuation coefficient images. Unlike Vermeer, we first averaged all eight B-scan repeats prior to calculating the attenuation coefficient to improve SNR. As described by Vermeer,

attenuation coefficient estimation algorithms can suffer from a depth-dependent bias related to the OCT axial point spread function. The bias correction factor requires knowledge of parameters Z, Z_0 and Z_R, where Z is the depth location of interest, Z_0 is the focus location and Z_R is Rayleigh range of the OCT center wavelength in tissue. For studies reported here, Z_0 was fixed and Z_R was 0.532 ± 0.00675 mm. Distance from the focal plane (Z_0) was computed by subtracting pixel numbers ($Z-Z_0$) and multiplying by the calibrated Z-pixel size (6.75 μm).

Shadowing from large vessels resulted in artificially reduced attenuation coefficient values in tissue regions underneath blood vessels. To remove this artifact, a mask was created from angiography images and applied to the tumor binary image (see section 3). This mask was the result of thresholding angiography images such that voxels with decorrelation values greater than 0.3 (i.e. regions with moving scattering centers) were set to 0 and all others set to 1. The angiography mask was multiplied by the tumor binary image so that any voxel classified as cancerous near a vessel was set to 0 and thus reclassified as non-cancerous (Figure S3). A binary fill operation was applied on the result to restore legitimate tumor regions that were masked due to vessel proximity. Figure S4 illustrates renderings of attenuation coefficient for four mice (#1, #2, #3 and #5). As reported in Section 3, a characteristic columnar region was observed in all mice corresponding to tumor growth along the needle track. Additionally, a wider underlying tumor region was observed along the boundary of the hippocampus and corpus callosum.

Limitations in confocal fluorescence microscopy tumor imaging: Vasculature and tumor locations in mice (#3, #5) were highlighted by using OCT images and maximum intensity Z-projections of fluorescence confocal microscopy. Figures S5 and S6 show the combined maximum intensity projection of the OCT angiography images (red) with thresholded OCT attenuation coefficient data (green) from the cortical surface down to about 2 mm for mice #3 and #5 respectively. In Figure S5, Panel C, tumor location starts at a depth of 300 μm (highlighted B-scan of Panel B). Vertical extent of the tumor in this location is around 500 μm. Tumor lateral dimensions in confocal fluorescence images are artifactually limited by a shallow penetration depth (Figure S5, Panel A). Similarly, in Figure S6, Panel C, the tumor margin extended 1.2 mm deep in the highlighted location. This depth confirms limitations of tumor visibility in fluorescence confocal imaging (Panel A). Complete rendered tumor volumes can be observed in Panel D of Figure S4.

Laser surgery results in additional mice: In addition to Figure 3, which shows coagulation on mouse #2, Figure S7 shows a coagulation zone cross-section. Pre-coagulation (red) and post-coagulation (green) angiography cross-sections when merged appear yellow (Figure S7 Panel A) in regions that are not coagulated and remain red where blood has been coagulated. White dotted lines in Panel A show cone of Tm laser (1.94 μm) coagulation. The conical shaped coagulation zone (white arrow) is shown in Panel B of Figure S7. Adjacent (to Figure 4) regions in mouse #4 (pre-ablation tumor margin shown in blue in Panels A and C) highlight the remaining nearby tumor regions and surrounding tissue post-ablation (gray) with corresponding histology images (Panels B, D respectively of Figure S8).

References:

1. Hale GM, Querry MR. Optical Constants of Water in the 200-nm to 200-μm Wavelength Region. Appl Opt 1973; 12: 555.

2. Jacques SL. Optical properties of biological tissues: A review. Phys Med Biol 2013; 58: 37–61.

3. Vogel A, Venugopalan V. Mechanisms of Pulsed Laser Ablation of Biological Tissues. Chem Rev 2003; 103: 577-644.

4. Katta N, McElroy AB, Estrada AD, Milner TE. Optical coherence tomography image-guided smart laser knife for surgery. Lasers Surg Med 2017; 50: 202-212.

5. Vakoc BJ, Lanning RM, Tyrrell J a, Padera TP, a L, Stylianopoulos T, Munn LL, Tearney GJ, Jain RK, Bouma BE. Three-dimensional microscopy of the tumor microenvironment in vivo using optical frequency domain imaging. Nat Med 2010; 15: 1219–1223.

6. Nolan RM, Adie SG, Marjanovic M, Chaney EJ, South FA, Monroy GL et.al. Intraoperative optical coherence tomography for assessing human lymph nodes for metastatic cancer. BMC Cancer 2016; 16: 144.

7. Jia Y, Tan O, Tokayer J, Potsaid B, Wang Y, Liu JJ et.al. Split-spectrum amplitude-decorrelation angiography with optical coherence tomography. Opt Express 2012; 20: 4710–4725.

8. Braaf B, Vermeer KA, Sicam VADP, van Zeeburg E, van Meurs JC, de Boer JF. Phase-stabilized optical frequency domain imaging at 1-μm for the measurement of blood flow in the human choroid. Opt Express 2011; 19: 20886–20903.

9. Potsaid B, Baumann B, Huang D, Barry S, Cable AE, Schuman JS,et.al. Ultrahigh speed 1050nm swept source/Fourier domain OCT retinal and anterior segment imaging at 100,000 to 400,000 axial scans per second," Opt Express 2010; 19: 20029–20048.

10. Chen C-L, Wang RK. Optical coherence tomography based angiography. Biomed Opt Express 2017; 8: 1056.

11. Yang M T, Chih-Chung, Ting-Ta CHL, Chang FY, Yang CH, Lee CK,et.al. Microvascular Imaging Using Swept-Source Optical Coherence Tomography with Single-Channel Acquisition. Appl Phys Express 2011; 4: 97001.

12. Mariampillai A, Leung MKK, Jarvi M, Standish BA, Lee K, Wilson BC,et.al. Optimized speckle variance OCT imaging of microvasculature. Opt Lett 2010; 35: 1257–1259.

13. Lo WCY, Uribe-Patarroyo N, Nam AS, Villiger M, Vakoc BJ, Bouma BE. Laser thermal therapy monitoring using complex differential variance in optical coherence tomography. J Biophotonics 2016; 10: 84–91.

14. Kut C, Chaichana KL, Xi J, Raza SM, Ye X, McVeigh ER,et.al. Detection of human brain cancer infiltration ex vivo and in vivo using quantitative optical coherence tomography. Sci Transl Med 2015; 7: 100-292.

15. Vermeer KA, Mo J, Weda JJA, Lemij HG, de Boer JF. Depth-resolved model-based reconstruction of attenuation coefficients in optical coherence tomography. Biomed Opt Express 2014; 5: 322–337.